Contents lists available at ScienceDirect

International Journal of Heat and Mass Transfer

journal homepage: www.elsevier.com/locate/ijhmt

Assessment of body force effects in flow condensation, Part I: Experimental investigation of liquid film behavior for different orientations

Ilchung Park, Lucas E. O'Neill, Chirag R. Kharangate, Issam Mudawar *

Boiling and Two-Phase Flow Laboratory (BTPFL), School of Mechanical Engineering, Purdue University, 585 Purdue Mall, West Lafayette, IN 47907, USA

ABSTRACT

Body force effects in flow condensation vary depending on channel orientation and fluid mass velocity, making the design of systems intended to operate in multiple orientations more complicated than those at a fixed orientation. This study examines the effects of body force on liquid film development for flow condensation of FC-72 in horizontal, vertical upflow, and vertical downflow orientations. Two test sections are utilized, one capable of providing high-speed imaging of liquid film development, and the other designed to allow detailed measurements of flow condensation heat transfer coefficient. High speed imaging shows that for low FC-72 mass velocities, flow regimes differ significantly among the three orientations, with vertical upflow exhibiting falling film behavior, horizontal flow showing stratification, and vertical downflow displaying annular co-current flow. For the case of low mass velocity horizontal flow, interfacial disturbances in the form of a sinusoidal wave are clearly visible with wavelengths on the order of 1–10 mm. As mass velocity is increased, the liquid film is seen to exhibit similar behavior for all three orientations due to interfacial shear stress negating body force effects. Heat transfer measurements reinforce these trends, with circumferential variations in heat transfer coefficient present for horizontal flow at low mass velocities, and differences in the axial variations in heat transfer coefficient seen when comparing vertical upflow to vertical downflow. As mass velocity is increased, differences in heat transfer coefficient are reduced, with the highest mass velocities exhibiting almost no variation with orientation. This convergence of values indicates the ability of interfacial shear stress to mitigate body force effects at sufficiently high mass velocities.

© 2016 Elsevier Ltd. All rights reserved.

1. Introduction

1.1. Importance of gravity to interfacial behavior and condensation heat transfer

In flow condensation, both pressure drop and heat transfer characteristics change significantly depending on flow regime. Numerous investigations that are dedicated to condensation flow regime identification can be found in the literature, with the vast majority focusing on flow regimes in horizontal tubes [1–8]. However, it has been shown that tube inclination angle has a strong influence on the distribution of liquid and vapor inside the tube, and therefore both flow regime and heat transfer coefficient during flow condensation [9]. It is therefore important to develop a more comprehensive understanding of the influence of gravity on interfacial behavior in flow condensation. This is particularly the case for the annular flow regime, which both provides the highest heat transfer coefficients and typically prevails over the longest axial span of a condensation tube as compared to all other condensation flow regimes combined.

Multiple approaches exist to investigate the effect of gravity, or the lack thereof, on flow condensation. Experimental data have been obtained in microgravity that is achieved in about 15-s durations in parabolic flight aircraft [10]. But the simplest and most cost effective approach is to perform condensation experiments in Earth gravity at different tube orientations. This allows test data for the different orientations to be compared, and the relative influence of gravity on flow regimes and condensation heat transfer carefully analyzed.

Several investigations have relied on adiabatic air–water experiments to construct a flow regime map for the entire range of channel orientations [11], investigate pressure drop in inclined tubes

Nomenclature

C	empirical constant		*Subscripts*	
c_p	specific heat at constant pressure		avg	average
D	tube diameter		bottom	bottom of tube's perimeter
G	mass velocity		f	liquid
g	gravity		FC	FC-72
h	heat transfer coefficient		g	vapor
h_{fg}	latent heat of vaporization		i	inner diameter
j^*	dimensionless superficial mass velocity		in	inlet to heat transfer measurement length
k	thermal conductivity		o	outer diameter
$\dot{m}$	mass flow rate		out	outlet of heat transfer measurement length
P	pressure		sat	saturation
q	rate of heat transfer from FC-72 to water		ss	stainless steel
Re_f	liquid film Reynolds number		top	top of tube's perimeter
T	temperature		w	water
x_e	thermodynamic equilibrium quality		wall	stainless steel tube wall
z	axial coordinate			

Greek symbols
ρ density

[12], and develop a correlation for void fraction for different orientations [13]. However, findings from these adiabatic studies are not directly applicable to condensing flows.

As indicated by Lips and Meyer [9], the number of studies addressing flow condensation for varying tube orientations is quite small. In one early investigation of the effects of channel inclination, Chato [14] showed that the heat transfer coefficient increases with increasing inclination angle during downflow condensation in tubes with a slight downward inclination due to decreased depth of liquid in the tube. Wang and Du [15] performed an experimental and theoretical investigation of laminar condensation in inclined tubes using steam as working fluid. They reported that the condensation heat transfer coefficient can be increased or decreased by changing the tube's inclination angle, depending on the tube diameter, vapor quality, and mass velocity. The results were explained by relating the effect of gravity to liquid film thickness. An analytical model was developed to predict the liquid–vapor interfacial shape for stratified flow, and heat transfer coefficients predicted by the model compared favorably with experimental results. Akhavan-Behabadi et al. [16] experimentally investigated the effects of inclination angle on flow condensation of R134a inside a microfin tube. Their work showed that heat transfer coefficients for downflow condensation are higher than those for upflow condensation. Nitheanandan and Soliman [17] performed experiments to investigate the influence of small inclination angles (±10°) on flow regime boundaries for steam condensation. The influence on the boundary of the annular flow regime was virtually insignificant, while even a small angle of inclination strongly influenced wavy and slug flow regime boundaries. Later, Nitheanandan and Soliman proposed a mechanistic model to predict the transition between stratified and non-stratified flows [18]. More recently, Lips and Meyer [19] performed an experimental study of R134a condensation over the entire range of tube orientations between vertical downflow to vertical upflow. They determined that the condensation heat transfer coefficient is dependent on flow regime, which in turn is dominated by a balance between gravitational force, interfacial shear, and surface tension. Flow images captured using a high-speed camera showed that the flow became annular and was unaffected by inclination angle at higher mass velocities with high vapor quality, where interfacial shear stress dominates gravitational force. On the other hand, inclination angle had a strong influence on flow regime at low mass velocities with low vapor quality.

In recent years, research shifted to condensation in mini/microchannels. Wang and Rose [20] constructed an analytical model to explore the effect of channel inclination on condensation of R134a in square micro-channels, where surface tension and surface curvature of the condensing film were accounted for, while inertia and convection terms were neglected. The model provided predictions for liquid film thickness, mean heat flux, and mean condensation heat transfer coefficient around the channel's perimeter for a range of channel inclinations varying from vertical downflow to vertical upflow. A theoretical and numerical analysis of stratified condensation of R141b, R11, and R134a by Saffari and Naziri [21] showed that condensation is strongly influenced by tube inclination angle, and an inclination of 30–50° above horizontal proved optimal for heat transfer. Da Riva and Del Col [22] numerically simulated condensation of R134a in a circular minichannel for horizontal flow and vertical downflow in Earth's gravity, and for vertical downflow in zero gravity. They showed that gravity effects were dominant at low mass velocities, resulting in higher heat transfer coefficients for horizontal flow than those for vertical downflow. But simulations for high mass velocities showed a substantial diminution in the gravity effects, with the liquid film flow dominated by interfacial shear.

1.2. Objectives of study

Clearly, the exact influence of gravity on flow condensation remains quite illusive, with no mechanistic guidelines available to ascertain when this influence may be neglected. These issues are the basis for the present two-part study. In this first part, the influence of gravity on flow condensation is isolated by conducting identical experiments at three different flow orientations: horizontal flow, vertical downflow, and vertical upflow, using FC-72 as working fluid. Two separate test modules are developed for this purpose. The first is used to conduct detailed high-speed video motion analysis of the flow characteristics, with particular attention paid to interfacial behavior, for different flow orientations. The second module is used to obtain detailed heat transfer

measurements to explore differences in condensation heat transfer coefficient among the three flow orientations resulting from variations in the mass velocities of FC-72 and cooling water. In the second part of this study [23], the experimental findings from this part are used to develop mechanistic criteria for negating the influence of gravity in condensing flows.

The present study is part of a joint project between the Purdue University Boiling and Two-Phase Flow Laboratory (PU-BTPFL) and NASA Glenn Research Center that was initiated in 2012 to develop the Flow Boiling and Condensation Experiment (FBCE) for eventual deployment on the International Space Station (ISS). The ultimate objectives of the project are to obtain flow boiling and condensation databases in microgravity, and to develop mechanistic models for flow boiling critical heat flux (CHF) and flow condensation in microgravity, as well as minimum flow rate criteria required to ensure gravity-independent CHF and condensation. While significant progress has been made by the joint Purdue-NASA team towards both predicting CHF and developing criteria for gravity-independent CHF [24–27], no such criteria have been developed for condensing flows. Developing the criteria for condensation is the primary objective of the present two-part study.

2. Experimental methods

2.1. Condensation facility

Fig. 1(a) shows a schematic diagram of the condensation facility; a photo of the facility is depicted in Fig. 1(b). The facility is comprised of three loops, a primary loop for the condensing fluid, FC-72, and two separate water cooling loops. The central component of the facility is the condensation module, where FC-72 vapor is partially condensed to liquid by rejecting heat to cooling water that is circulated using the first water loop. A separate condenser installed downstream of the test module uses the second water loop to achieve additional condensation of the FC-72 vapor.

FC-72 is a colorless and odorless dielectric perfluorinated fluid that is manufactured by 3M Company and marketed mostly for electronics cooling applications. Table 1 provides representative thermophysical properties for both FC-72 and water at 66.4 °C, which is the saturation temperature of FC-72 at a representative operating pressure of this study of 1.40 bar.

Most of the FC-72 liquid is contained in a sealed liquid reservoir in the primary loop. Liquid FC-72 is pumped through the primary loop with the aid of a gear pump. The liquid is first passed through one of several rotameters connected in parallel for flow rate measurement. The liquid continues to a 14.2-kW Watlow pre-heater, where it is converted to slightly superheated vapor. The superheated FC-72 then enters the condensation test module, where it is partially returned to liquid state by rejecting heat to a counterflow of cooling water provided by the first water loop. Notice that the condensation module can be mounted in any direction relative to gravity; the FC-72 flow orientations tested in this study are vertical downflow, vertical upflow and horizontal flow. The two-phase mixture of FC-72 exiting the condensation module is routed into a plate-type condenser, where further condensation is achieved by rejecting heat to cooling water provided by the second water loop. Any remaining FC-72 vapor is converted to subcooled liquid using an air-cooled condenser before returning to the reservoir.

Shown in Fig. 1(a), the first water cooling loop absorbs heat from the FC-72 in the condensation module using a 14-kW modular Lytron cooling system, which is comprised of a reservoir, a pump and a liquid-to-liquid heat exchanger; the latter is used to reject the heat to tap water. The second water cooling loop uses a 1.46-kW modular Lytron cooling system, which is comprised of reservoir, a pump, and a water-to-air heat exchanger.

Prior to performing any measurements, a very thorough deaeration protocol is followed to rid the FC-72 from any dissolved noncondensable gases. The FC-72 is vigorously boiled for 30 min using two 300-W immersion heaters situated at the bottom of the primary loop's reservoir, while simultaneously condensing the FC-72 and gradually purging any non-condensable to the ambient.

Pressure and temperature sensors are located throughout the facility. FC-72 temperature is measured at the inlets of both rotameters and the pre-heater. The FC-72 temperature and pressure are measured at the inlet and outlet of the condensation module. Similarly, the temperature and pressure of the cooling water are measured at the inlet and outlet of the condensation module. In addition, the temperatures of the FC-72 and cooling water are measured at multiple locations along the condensation module as will be discussed below.

2.2. Condensation module for flow visualization

Two separate condensation test modules are used in this study: one for flow visualization purposes, and the other for heat transfer measurements. The two modules feature similar dimensions, but are constructed using different materials to facilitate image capture in the first and accurate heat transfer measurement in the second.

Fig. 2(a) illustrates the construction of the condensation module for flow visualization, which features a transparent tube-in-tube construction. The FC-72 flows through the inner tube while the water flows in counter-flow through the annulus between the inner and outer tubes. The inner 1219-mm long borosilicate glass tube has a 10.16-mm inner diameter and wall thickness of 1.8 mm. The outer polycarbonate plastic (Lexan) tube, which features high transparency but very low thermal conductivity, has a 19.05-mm inner diameter and an outer diameter of 24.4 mm. Short latex rubber sleeves are secured between the inner and outer tubes at both the inlet and outlet of the condensation module, resulting in a 1143-mm condensation length for flow visualization. Type-T thermocouples and pressure transducers are installed at the FC-72 inlet and outlet of the flow visualization module. Both the inlet and outlet of the water side are also fitted with type-T thermocouples.

Flow visualization is performed using a high-speed Photron Fastcam Untima APX video camera system. The camera is mounted normal to the front of the condensation module for all three FC-72 flow orientations tested: vertical downflow, vertical upflow and horizontal flow. The camera is fitted with an assortment of lens attachments and light sources to provide optimum image quality for each orientation. For vertical downflow, infinity K2/SC long-distance microscope lenses are used along with high intensity back-lighting from an incandescent bulb. For the vertical upflow and horizontal flow orientations, the video camera is fitted with a Nikon 105-mm F/2.8D magnification lens, with lighting provided by an array of 15 high power white 5-W LEDs.

Flow visualization experiments are performed at the inlet, middle, and outlet regions of the condensation length, which are centered at 190, 571 and 952 mm, respectively, from the FC-72 inlet of the module, for all three flow orientations. Video segments are captured at a rate of 4000 frames/s for the vertical downflow orientation, and 8000 frames/s for horizontal flow and vertical upflow.

2.3. Condensation module for heat transfer measurements

The second condensation module is designed to facilitate detailed heat transfer measurements. The overall design of this module is very similar to that of the flow visualization module, but constructed with different materials to ensure heat transfer measurement accuracy. Fig. 2(b) illustrates the construction of
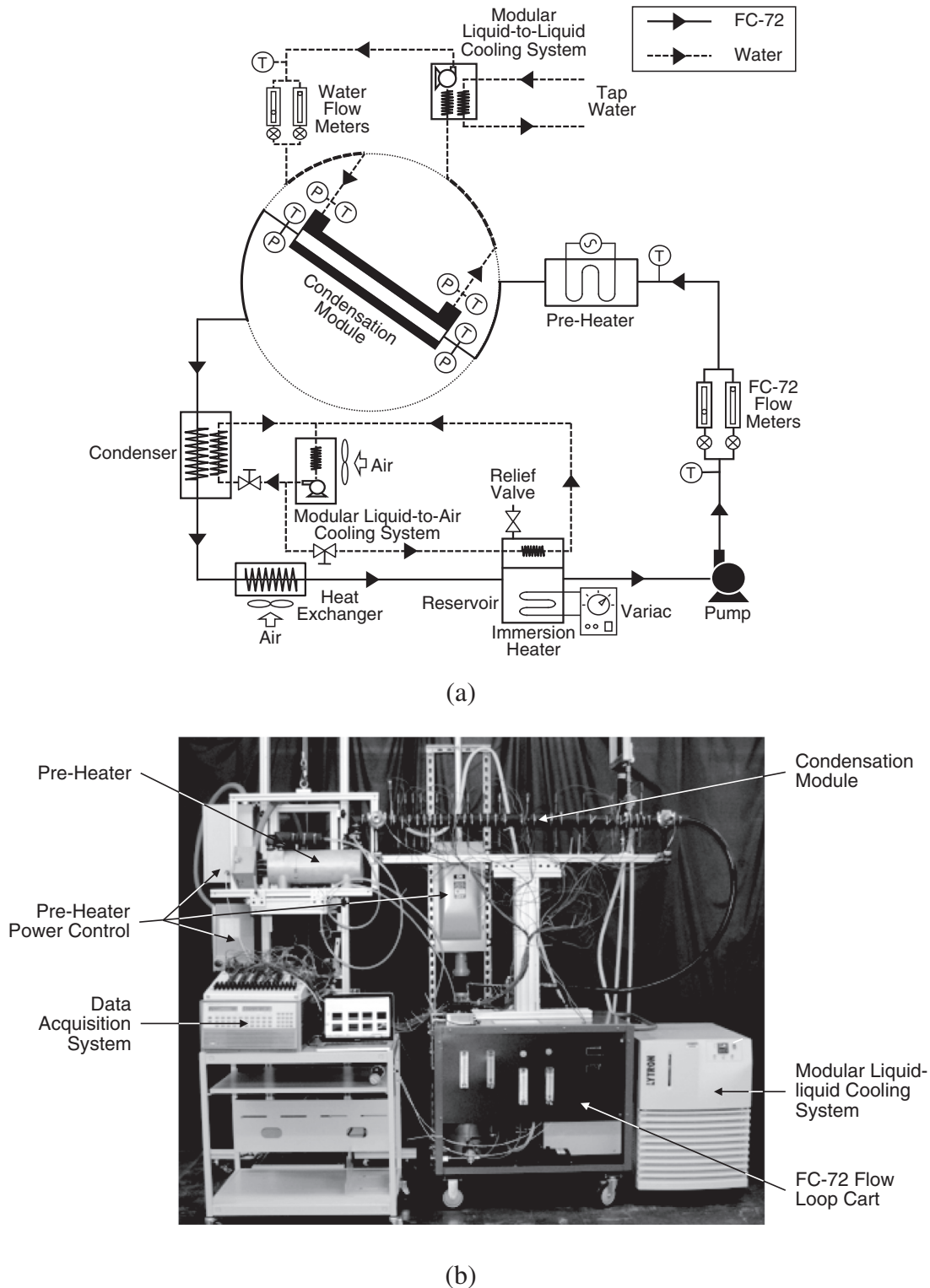
(a)

(b)

Fig. 1. (a) Schematic diagram and (b) photo of condensation facility.

the condensation module for heat transfer measurements, which features a condensation length of 1259.8 mm. Both inner and outer tubers are made from 304 stainless steel. The inner tube has an inner diameter of 11.89 mm and 0.41-mm wall thickness, and the outer tube has an inner diameter of 22.48 mm and 3.05-mm wall thickness. A key goal in the construction of this module is to achieve a compromise between minimizing resistance to radial heat conduction from the condensing FC-72 to the water, and minimizing axial conduction effects along the direction of fluid flow. This compromise is achieved by the combination of small wall thickness of the inner tube and relatively low thermal conductivity of stainless steel. Heat losses to the ambient are minimized by encasing the entire module with a thick layer of fiberglass insulation.

Table 1
Thermophysical properties of saturated FC-72 and water at 66.4 °C corresponding to FC-72 saturation pressure of 1.40 bar.

	k_f [W/m K]	μ_f [kg/m s]	$c_{p,f}$ [J/kg K]	σ [mN/m]	h_{fg} [kJ/kg]	ρ_f [kg/m³]	ρ_g [kg/m³]
FC-72	0.0527	391×10^{-6}	1234	7.39	92	1567	18.14
Water	0.6466	425×10^{-6}	4185	65.12	2342	980	0.17

The condensation module for heat transfer measurements features the same temperature and pressure instrumentation at the inlets and outlets of both FC-72 and water but contained 45 additional type-T thermocouples. As shown in Fig. 2(c), 28 thermocouples are installed in 14 diametrically opposite pairs on the outer surface of the inner tube. Thermocouple beads are brazed to the outer surface to minimize contact resistance and ensure contact with the surface is maintained during flow. Use of thermocouple pairs is intended to detect any asymmetry in the wall temperatures for vertical downflow and upflow orientations, while also enabling the capture of temperature differences between the top and bottom surfaces of the inner tube at the same axial location due to gravity effects for the horizontal flow orientation. 14 additional thermocouples are inserted into the annulus at the same axial locations as the wall thermocouples to measure water temperatures. An additional thermocouple is mounted at each of three of the 14 water thermocouple locations diametrically opposite to the main thermocouples to capture any asymmetry in the water temperatures. The layout of all 45 thermocouples is illustrated in Fig. 2 (c). The axial distance between FC-72 thermocouple pairs is 38.1 mm in the FC-72 inlet region, and 76.2 and 139.7 mm in the middle and outlet regions, respectively. All 45 thermocouples are made from 0.21 mm diameter thermocouple wire and possess a bead diameter of 0.79 mm.

2.4. Operating conditions and measurement uncertainty

Two separate series of experiments are conducted using the two condensation modules for each of the three different flow orientations: vertical downflow, vertical upflow, and horizontal flow. The experiments performed using the flow visualization module aim at identifying dominant condensation flow regimes and capturing the detailed interfacial behavior of the condensing film for the different orientations. The second set of experiments conducted using the condensation module for heat transfer measurements is intended to obtain detailed heat transfer measurements and investigate the difference in heat transfer characteristics among the three flow orientations. For both series of experiments, the thermodynamic equilibrium quality of FC-72 at the inlet of the condensation module is maintained slightly above unity.

The flow visualization experiments for vertical downflow, vertical upflow, and horizontal flow condensation consist of 40, 65, and 110 operating conditions, respectively. Summarized in Table 2, the 40 operating conditions for vertical downflow include five FC-72 mass velocities in the range of G_{FC} = 19.21–136.54 kg/m²s and eight different water mass velocities for each FC-72 mass velocity in the range of G_w = 12.75–146.92 kg/m²s. For vertical upflow, the 65 operating conditions are comprised of nine FC-72 mass velocities in the range of G_{FC} = 13.32–159.49 kg/m²s and a broad range of water mass velocities of G_w = 6.09–977.79 kg/m²s. Finally, the 110 operating conditions for horizontal flow are comprised of 22 FC-72 mass velocities in the range of G_{FC} = 26.65–343.79 kg/m²s and water mass velocities of G_w = 12.22–476.64 kg/m²s. Table 2 also provides values of inlet quality, $x_{e,in}$, inlet temperature, $T_{FC,in}$, and inlet pressure, $P_{FC,in}$ of FC-72 for all three flow orientations. Also included in the same table are the amount of heat transferred from FC-72 to the cooling water, q, outlet thermodynamic equilib-

rium quality of FC-72, $x_{e,out}$, and outlet FC-72 film Reynolds numbers, $Re_{f,out}$.

The test matrices for heat transfer measurements are identical for all three flow orientations, with each consisting of 39 operating conditions. As indicated in Table 3, tests for each flow orientation include 13 FC-72 mass velocities in the range of G_{FC} = 116.80–576.83 kg/m²s and three different water mass velocities of G_w = 246.66, 277.48, and 308.32 kg/m²s for each FC-72 mass velocity. To exclude potential uncertainties associated with cooling water entrance effects, heat transfer data are captured only within the upstream condensation length of z = 0–807.7 mm. The inlet quality of FC-72 is slightly superheated, with $x_{e,in}$ = 1.03–1.07, 1.04–1.09, and 1.03–1.07 for horizontal flow, vertical downflow, and vertical upflow, respectively. These superheated inlet conditions resulted in upstream single-phase superheated vapor regions of 19.39–77.54 mm (2.40–9.60% of the 807.7-mm length adopted in the heat transfer measurements), 22.62–75.93 mm (2.80–9.40% of the measurement length), and 16.15–66.23 mm (2.0–8.2% of the measurement length) for horizontal flow, vertical downflow, and vertical upflow, respectively. The inlet temperature and pressure of FC-72 for all three orientations fall in the ranges of $T_{FC,in}$ = 63.06–84.46 °C and $P_{FC,in}$ = 99.73–205.0 kPa, respectively, with the amount of heat transferred between the FC-72 and water varying from 916.47 to 3071.25 W. A saturated two-phase mixture is maintained at the exit of the heat transfer measurement length for all operating conditions, with FC-72 outlet thermodynamic qualities of $x_{e,out}$ = 0.01–0.53, 0.01–0.52 and 0.24–0.52 for horizontal flow, vertical downflow, and vertical upflow, respectively. The corresponding outlet film Reynolds numbers are $Re_{f,out}$ = 2624.79–7424.95, 2617.58–7600.17, and 1913.39–7792.72 for horizontal flow, vertical downflow, and vertical upflow, respectively.

The uncertainties of the pressure transducers and thermocouples used throughout the condensation facility are ±0.5% and ±0.4 °C, respectively. The outer diameter and wall thickness of the condensing tube used for the heat transfer measurements possess uncertainties of ±0.08 and ±0.03 mm, respectively. Uncertainties in the outer diameter and wall thickness of the outer tube for the same condensation module are ±0.13 and ±0.18 mm, respectively. Combining all these uncertainties with those associated with determination of fluid properties results in overall uncertainties in determining heat transfer rate, vapor quality, and condensation heat transfer coefficient of ±9.87%, ±10.93%, and ±11.23%, respectively, for all three flow orientations.

3. Flow visualization results

Prior to discussing the results obtained from the condensation module for flow visualization, it is important to note that the captured video images represent two separate interfaces overlaid upon one another. This is because the FC-72 liquid film covers the entire inner perimeter of the condensing tube. This limitation complicates detailed quantitative assessment of the liquid film's interfacial structure for certain operating conditions.

Figs. 3–5 compare, for horizontal flow, vertical downflow, and vertical upflow, image sequences of the condensing film for relatively low, medium and high values of G_{FC}, respectively. The images presented have resolutions of 512 × 344, 1024 × 512, and
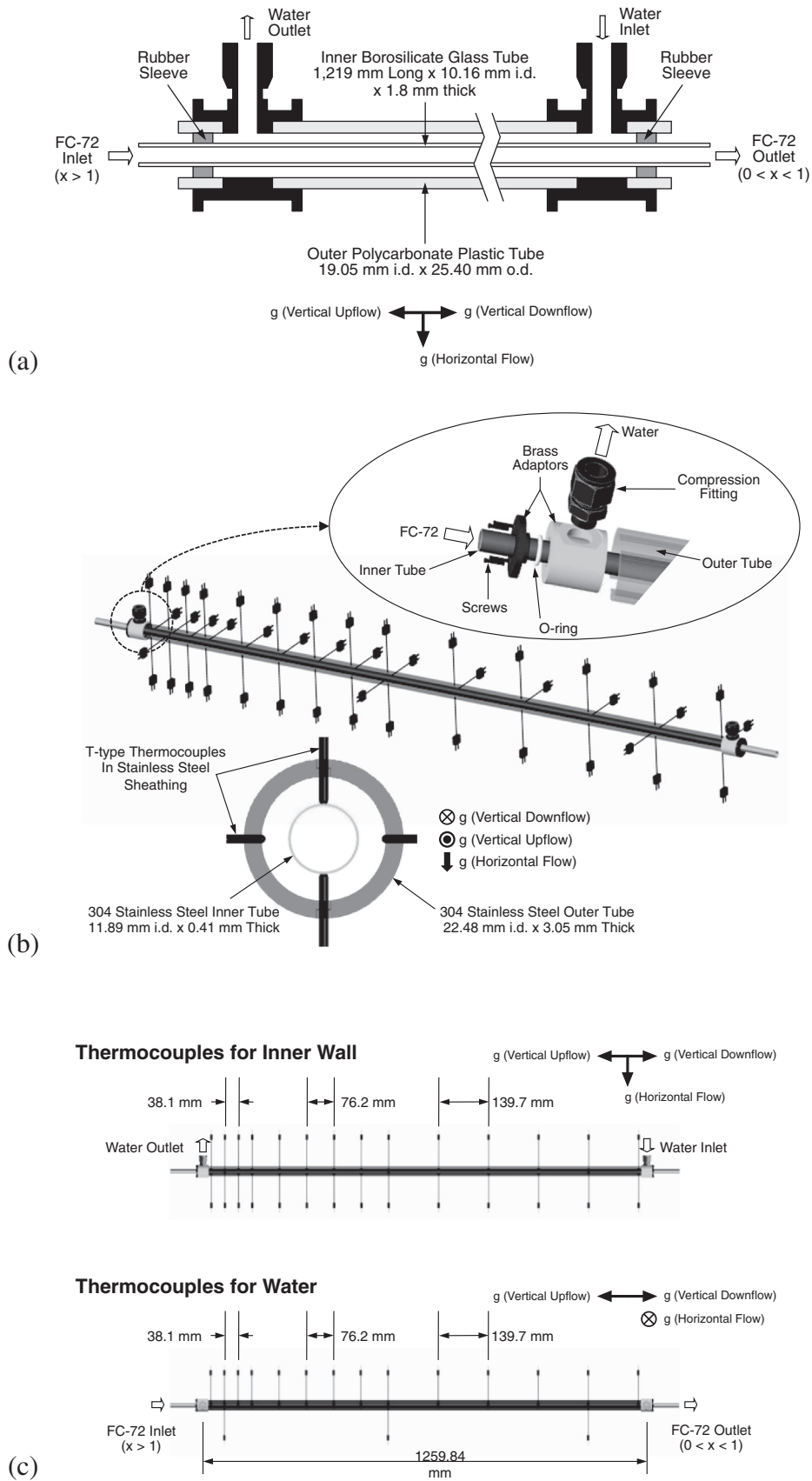
Fig. 2. (a) Construction of flow visualization module. (b) Construction of heat transfer module. (c) Location of thermocouples for temperature measurements of outer wall of inner tube and cooling water in heat transfer module.

Table 2
Experimental operating conditions for flow visualization tests.

		Horizontal flow		Vertical downflow		Vertical upflow	
		Max.	Min.	Max.	Min.	Max.	Min.
FC-72	$x_{e,in}$	1.12	1.03	1.03	1.00	1.14	1.00
	$\dot{m}_{FC}$ [g/s]	27.89	2.16	11.07	1.56	12.93	1.08
	G_{FC} [kg/m^{2}s]	343.79	26.65	136.54	19.24	159.49	13.32
	$T_{FC,in}$ [°C]	73.38	64.79	66.93	55.56	72.93	57.41
	$P_{FC,in}$ [kPa]	147.37	105.50	171.93	133.89	114.01	102.00
Cooling water	$\dot{m}_w$ [g/s]	64.97	1.67	20.03	1.74	133.29	0.83
	G_w [kg/m^{2}s]	476.64	12.22	98.21	8.53	977.79	6.09
	ΔT_w [°C]	26.14	3.01	30.06	2.87	23.29	1.14
q [W]		836.35	182.12	536.40	154.40	702.48	80.85
$x_{e,out}$		0.80	0.05	0.80	0.00	0.70	0.00
$Re_{f,out}$		2508.22	534.52	1741.82	355.54	1751.90	239.50

256×512 pixels for horizontal flow, vertical downflow, and vertical upflow, respectively. The actual length of the captured region for horizontal flow is 35.74 mm, and the actual heights of the captured regions for vertical downflow and vertical upflow are 6.69 and 40.80 mm, respectively. The total duration of each sequence in Figs. 3–5 is 0.3 s, with the individual images in a sequence separated by 0.0125 s.

3.1. Liquid film behavior for varying orientations and mass velocities

Fig. 3 shows representative sequential images of the condensing FC-72 film along the inner wall of the glass tube captured in the middle region of the same tube, centered at z = 571 mm, for relatively low FC-72 mass velocities and all three flow orientations. Fig. 3(a) depicts images captured during horizontal flow for G_{FC} = 39.94 kg/m^{2}s and G_w = 45.83 kg/m^{2}s. Due to the velocity difference between vapor and liquid phases, interfacial instabilities are clearly identifiable in the figure. However, the amplitude of the interfacial waves is too small to ensure any appreciable liquid contact with the top of the condensation tube. The liquid is shown accumulating along the bottom of the tube and forming a thick liquid layer, which demonstrates that the influence of gravity is significant at low FC-72 mass velocities. Fig. 3(b) shows images captured during vertical downflow condensation for G_{FC} = 38.48 - kg/m^{2}s and G_w = 41.98 kg/m^{2}s. The film appears relatively smooth and laminar, marred only by a few surface ripples. With the gravitational force acting in the same direction as the FC-72 flow, circumferential symmetry is achieved, and the film thickness is fairly uniform along the inner wall. Flow images captured during vertical upflow condensation for G_{FC} = 39.96 kg/m^{2}s and G_w = 45.85 kg/m^{2}s are presented in Fig. 3(c). Because of low FC-72 mass velocity, the liquid film moves opposite to the direction of the vapor core. This is classified as *falling film* behavior, which occurs when the vapor velocity is low and the influence of gravity on liquid motion significant. The liquid appears to behave as a well separated annular film over only brief intervals. Some of the liquid is shattered from the annular film in the form of ligaments and droplets, which are partly entrained upwards in the vapor core, or deposited back onto the liquid film. This produces brief intervals of well mixed two-phase flow consisting of a chaotic combination of falling film, upward moving vapor core, vapor bubbles entrained in the liquid, and liquid ligaments and droplets entrained in the vapor core. This chaotic mixture is then quickly replaced by the initial, well separated annular film, and the process is repeated in a cyclical manner. In vertical upflow, the motion of the annular liquid film is governed by the relative magnitude of the shear stress created by the upward moving vapor core and the gravitational force acting in the opposite direction, and the behavior depicted

in Fig. 3(c) is representative of relatively weak vapor shear. Comparing Fig. 3(a)–(c) reveals drastic differences in liquid film behavior for the different flow orientations, which is brought about by the relatively strong influence of gravity at low FC-72 mass velocities.

Fig. 4 shows representative image sequences corresponding to moderate FC-72 mass velocities for all three flow orientations. These images are captured in the outlet region, centered at z = 952 mm. For horizontal flow with G_{FC} = 79.78 kg/m^{2}s and G_w = 73.32 kg/m^{2}s, Fig. 4(a) shows the increase in FC-72 mass velocity from the low value corresponding to Fig. 3(a) renders the vapor shear strong enough to spread the liquid along the entire tube circumference. Gravity effects are still prevalent, which is evidenced by the much thicker liquid film at the bottom of the tube compared to the top. Notice also how the thicker film at the bottom leads to accumulation of liquid into larger waves compared to only small ripples along the top. Fig. 4(b) shows flow images for vertical downflow condensation with G_{FC} = 89.96 kg/m^{2}s and G_w = 83.95 kg/m^{2}s. Increasing the mass velocity of FC-72 compared to that corresponding to Fig. 3(b) is shown yielding higher interfacial shear and increased turbulence, which are manifest in more appreciable interfacial instabilities compared to those depicted in Fig. 3(b). Fig. 4(c) shows flow images representative of *climbing film* behavior for G_{FC} = 79.93 kg/m^{2}s and G_w = 73.36 kg/m^{2}s, which occurs during vertical upflow condensation as G_{FC} is increased from the value corresponding to Fig. 3(c). Here, the liquid film is shear-driven upwards, with the interface marred by ripples and large waves, which are induced by the high vapor shear. Comparing Fig. 4(a)–(c) reveals varied film behavior for the different flow orientations in the moderate range of FC-72 mass velocities as well.

Fig. 5 shows flow images captured in the inlet region, centered at z = 190 mm, at high FC-72 mass velocities for all three flow orientations. Increasing G_{FC} increases the mass velocity of the vapor core and therefore the interfacial shear stress, which begins to dwarf the influence of gravity. This can be seen in the images depicted in Fig. 5(a) for horizontal flow with G_{FC} = 132.95 kg/m^{2}s and G_w = 122.21 kg/m^{2}s. Notice how the liquid film is spread fairly uniformly along the inner perimeter, with the film motion dominated by the large vapor shear, and exhibiting interfacial instabilities. As shown in Fig. 5(b) and (c) for vertical downflow with G_{FC} = 136.51 kg/m^{2}s and G_w = 125.93 kg/m^{2}s, and vertical upflow with G_{FC} = 132.97 kg/m^{2}s and G_w = 122.21 kg/m^{2}s, respectively, the behavior of the liquid film is similar to that encountered in horizontal flow. Comparing Fig. 5(a)–(c) shows that the impact of flow orientation on film behavior is insignificant at high FC-72 mass velocities, as increased vapor shear appears to negate the influence of gravity.

Table 3
Experimental operating conditions for condensation heat transfer tests.

		Horizontal flow		Vertical downflow		Vertical upflow	
		Max.	Min.	Max.	Min.	Max.	Min.
FC-72	$x_{e,in}$	1.07	1.03	1.09	1.04	1.07	1.03
	$\dot{m}_{FC}$ [g/s]	64.02	12.96	63.95	12.97	63.97	12.96
	G_{FC} [kg/m^{2}s]	576.83	116.80	576.28	116.90	576.40	116.90
	$T_{FC,in}$ [°C]	83.70	63.53	84.03	62.39	84.46	63.06
	$P_{FC,in}$ [kPa]	200.61	109.16	201.77	99.73	205.00	114.44
Cooling water	$\dot{m}_w$ [g/s]	83.31	66.64	83.31	66.64	83.31	66.64
	G_w [kg/m^{2}s]	308.32	246.65	308.33	246.64	308.32	246.65
	ΔT_w [°C]	10.46	3.66	10.6	3.88	10.58	2.69
	q [W]	3009.29	1241.69	3071.25	1349.10	3067.06	916.47
	$x_{e,out}$	0.53	0.01	0.52	0.01	0.52	0.24
	$Re_{f,out}$	7424.95	2624.79	7600.17	2617.58	7792.72	1913.39

3.2. Identification and measurement of interfacial features

As mentioned earlier, the condensing film's coverage of the entire inner surface renders systematic quantitative analysis of the film's interfacial structure quite elusive. In particular, interfacial features are not clearly identifiable for vertical upflow and vertical downflow, so analysis of the corresponding images is not performed. However, detailed analysis of the film's interfacial structure is possible in horizontal flow at low and moderate mass velocities, where the liquid film covers only the lower portion of the tube. In particular, it is possible to characterize the wavelengths exhibited by the interfacial disturbances for these horizontal flow conditions.

To accomplish this task, flow images are imported into the 2-D drafting software DraftSight. This software is capable of using image boundaries as drawing elements, allowing a clear scale to be established for each imported frame. Then, by selectively identifying consecutive, clearly defined wave peaks, accurate measurement of the distance between peaks can be made.

Fig. 6 shows six horizontal flow images that are selected for analysis, with Fig. 6(a) consisting of four images for the lowest mass velocity (G_{FC} = 39.94 kg/m^{2}s), and Fig. 6(b) two images for the moderate mass velocity (G_{FC} = 79.78 kg/m^{2}s). The smaller sample size associated with G_{FC} = 79.78 kg/m^{2}s is the result of the film beginning to spread around the circumference of the inner tube, inhibiting the capture of clear interfacial features. Overall, the presence of a body force perpendicular to the interface produces larger, clearly identifiable interfacial waves for low and moderate mass velocities in horizontal flow than in vertical downflow and vertical upflow, which represents a significant conclusion in itself.

Fig. 6(a) shows horizontal flow at the lowest mass velocity of G_{FC} = 39.94 kg/m^{2}s yields interfacial features with wavelengths in the range of λ = 3.63–6.47 mm. On the other hand, Fig. 6(b), corresponding to horizontal flow at the moderate mass velocity of G_{FC} = 79.78 kg/m^{2}s, shows wavelengths fall in the range of 2.83–4.83 mm. This reveals a tendency for wavelengths to decrease with increasing mass velocity of FC-72. These values provide a physical baseline for expected wavelengths of interfacial features, which will be addressed in the second part of the present study [23].

4. Heat transfer results

4.1. Data reduction technique

As discussed in [28], a thermal model is constructed as illustrated in Fig. 7 to determine the local condensation heat transfer coefficient in the condensation module intended for heat transfer measurements. It is assumed that the liquid film interface is maintained at saturation temperature, T_{sat} (z), which in turn is deter-

mined from the pressure measurements. Accounting for the fact that pressure drop along the condensation length is very small, the saturation pressure, P_{sat} (z), which is used to determine T_{sat} (z), is calculated from a linear curve fit using the measured inlet and outlet pressures, P_{in} and P_{out}, respectively. The water temperature, T_w (z), and outer wall temperature of the inner tube, $T_{wall,o}$ (z), are determined from curve fits to their corresponding measured values. For the two-phase region of the condensation length where x_e < 1, the local condensation heat transfer coefficient, $h(z)$, of FC-72 is determined from:

$$dq = (\pi D_i dz)h(T_{sat} - T_{wall,i}) = \frac{T_{wall,i} - T_{wall,o}}{\frac{\ln(D_o/D_i)}{2\pi k_{ss}dz}} = \dot{m}_w c_{p,w} dT_w, \qquad (1)$$

where dq is the differential amount of heat transferred from the FC-72 to the water, which is computed from the differential rise in sensible energy of the water.

For the short upstream superheated region preceding the initiation of the liquid film, the temperature of FC-72 vapor, T_g (z), is obtained from the simple energy balance $\dot{m}_{FC} c_{p,g} dT_g = \dot{m}_w c_{p,w} dT_w$. For the same superheated region, x_e is computed from $x_e = 1 + c_{p,g}(T_g - T_{sat})/h_{fg}$, which is also used to determine the axial location where $x_e = 1$. The heat transfer coefficient for the superheated region is calculated by substituting T_{sat} in Eq. (1) with the local temperature of the superheated FC-72 vapor, T_g (z).

$$dq = (\pi D_i dz)h(T_g - T_{wall,i}) = \frac{T_{wall,i} - T_{wall,o}}{\left[\frac{\ln(D_o/D_i)}{2\pi k_{ss}dz}\right]} = \dot{m}_w c_{p,w} dT_w. \qquad (2)$$

For two-phase region where x_e < 1, the local mass flow rate of the FC-72 liquid film, $\dot{m}_f(z)$, is calculated by using the relation $d\dot{m}_f = dq/h_{fg}$ starting with the axial location where $x_e = 1$. The local thermodynamic equilibrium quality in the same region is determined by using $x_e = (\dot{m}_{FC} - \dot{m}_f)/\dot{m}_{FC}$.

4.2. Determination of local flow regimes

As the condensation module intended for heat transfer measurements is constructed from concentric stainless steel tubes, this module does not allow visual access to the condensing flow to determine dominant flow regimes. Therefore, the measured heat transfer coefficient is related to different flow regimes using previously developed flow regime transition criteria.

For horizontal flow condensation, the local flow regimes for the heat transfer results presented hereafter are determined using flow regime transition boundaries based on dimensionless superficial vapor velocity, $j_g^* = x_e G_{FC}/\sqrt{gD_i\rho_g(\rho_f - \rho_g)}$ [29]. These transitions can be summarized as: *stratified* for $j_g^* < 0.28$, stratified to wavy stratified for $0.28 \leqslant j_g^* < 1.61$, wavy stratified to wavy-annular
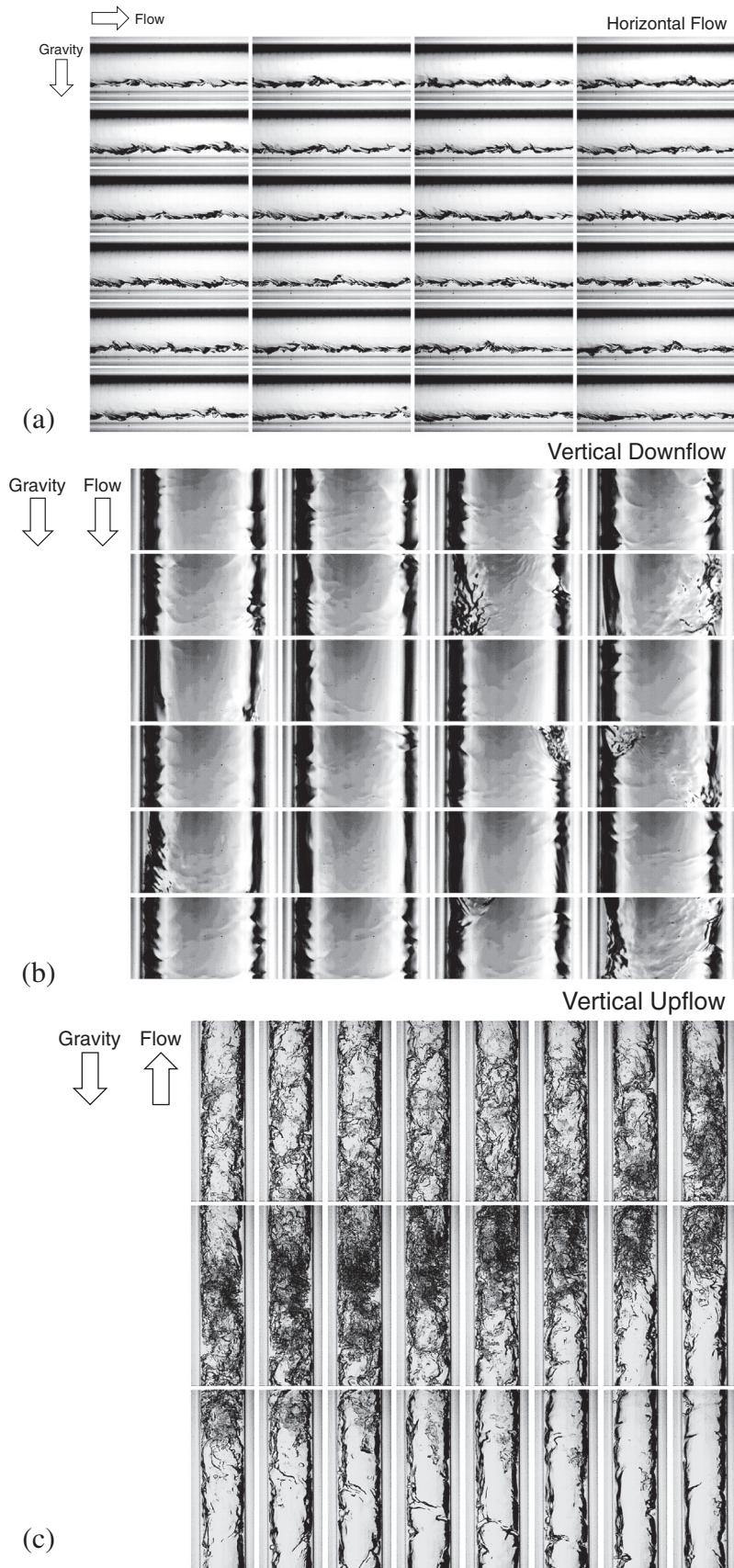
Fig. 3. Sequential images of condensing flow for relatively low FC-72 mass velocities of (a) G_{FC} = 39.94 kg/m^2 s with G_w = 45.83 kg/m^2 s for horizontal flow, (b) G_{FC} = 38.48 kg/m^2 s with G_w = 41.98 kg/m^2 s for vertical downflow, and (c) G_{FC} = 39.96 kg/m^2 s with G_w = 45.85 kg/m^2 s for vertical upflow. The total duration of each sequence is 0.3 s, with individual images separated by 0.0125 s.
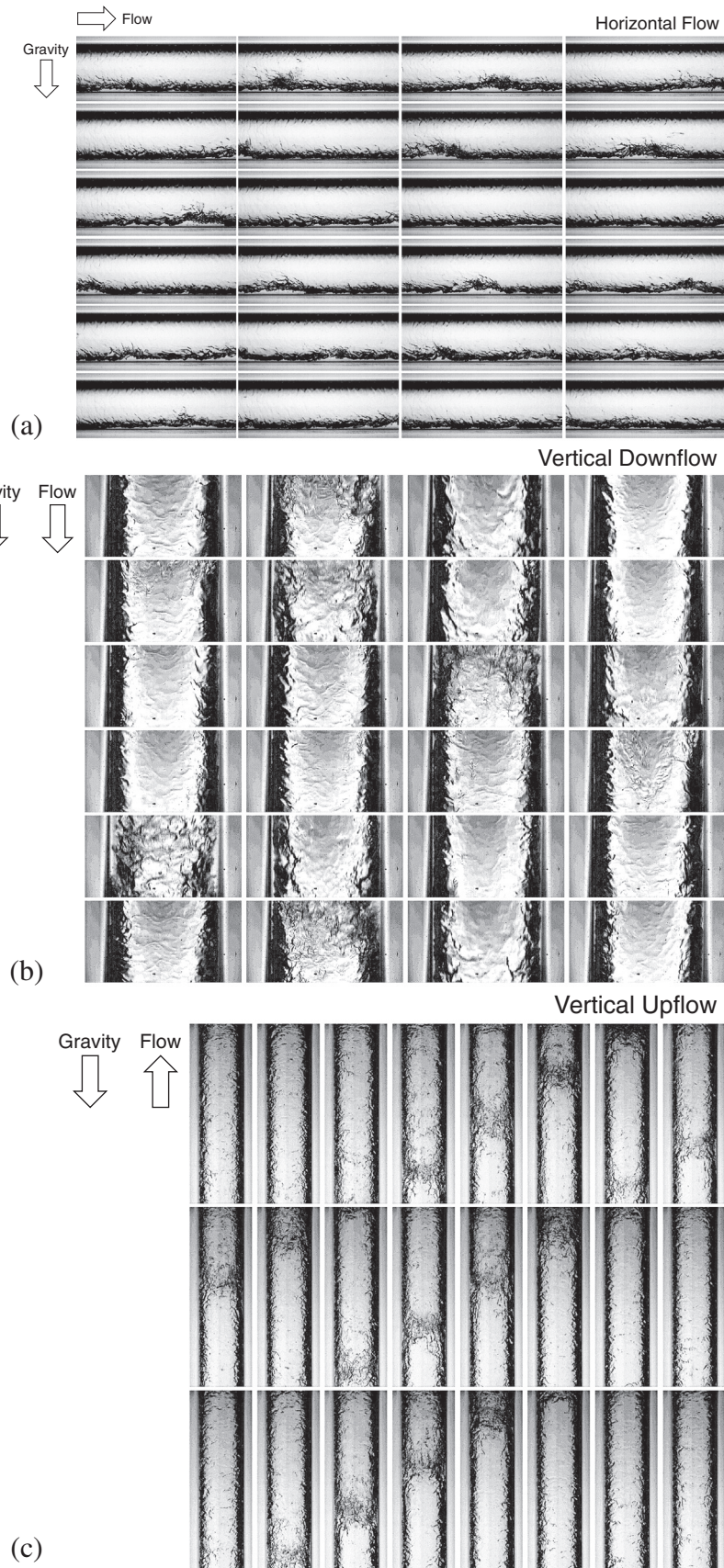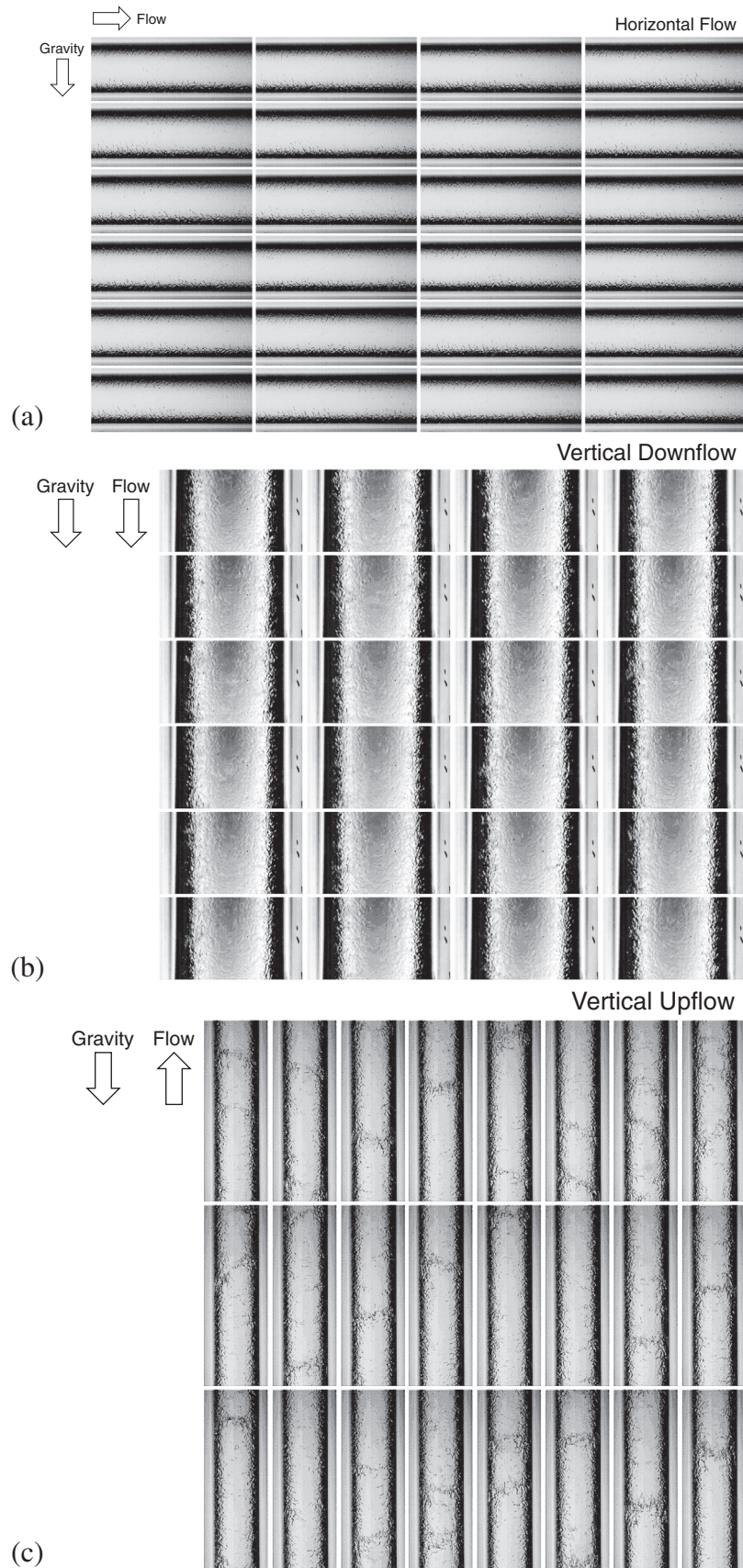
Fig. 4. Sequential images of condensing flow for relatively moderate FC-72 mass velocities of (a) G_{FC} = 79.78 kg/m² s with G_w = 73.32 kg/m² s for horizontal flow, (b) G_{FC} = 89.96 kg/m² s with G_w = 83.95 kg/m² s for vertical downflow, and (c) G_{FC} = 79.93 kg/m² s with G_w = 73.36 kg/m² s for vertical upflow. The total duration of each sequence is 0.3 s, with individual images separated by 0.0125 s.

Fig. 5. Sequential images of condensing flow for relatively high FC-72 mass velocities of (a) G_{FC} = 132.95 kg/m² s with G_w = 122.21 kg/m² s for horizontal flow, (b) G_{FC} = 136.51 kg/m² s with G_w = 125.93 kg/m² s for vertical downflow, and (c) G_{FC} = 132.97 kg/m² s with G_w = 122.21 kg/m² s for vertical upflow. The total duration of each sequence is 0.3 s, with individual images separated by 0.0125 s.
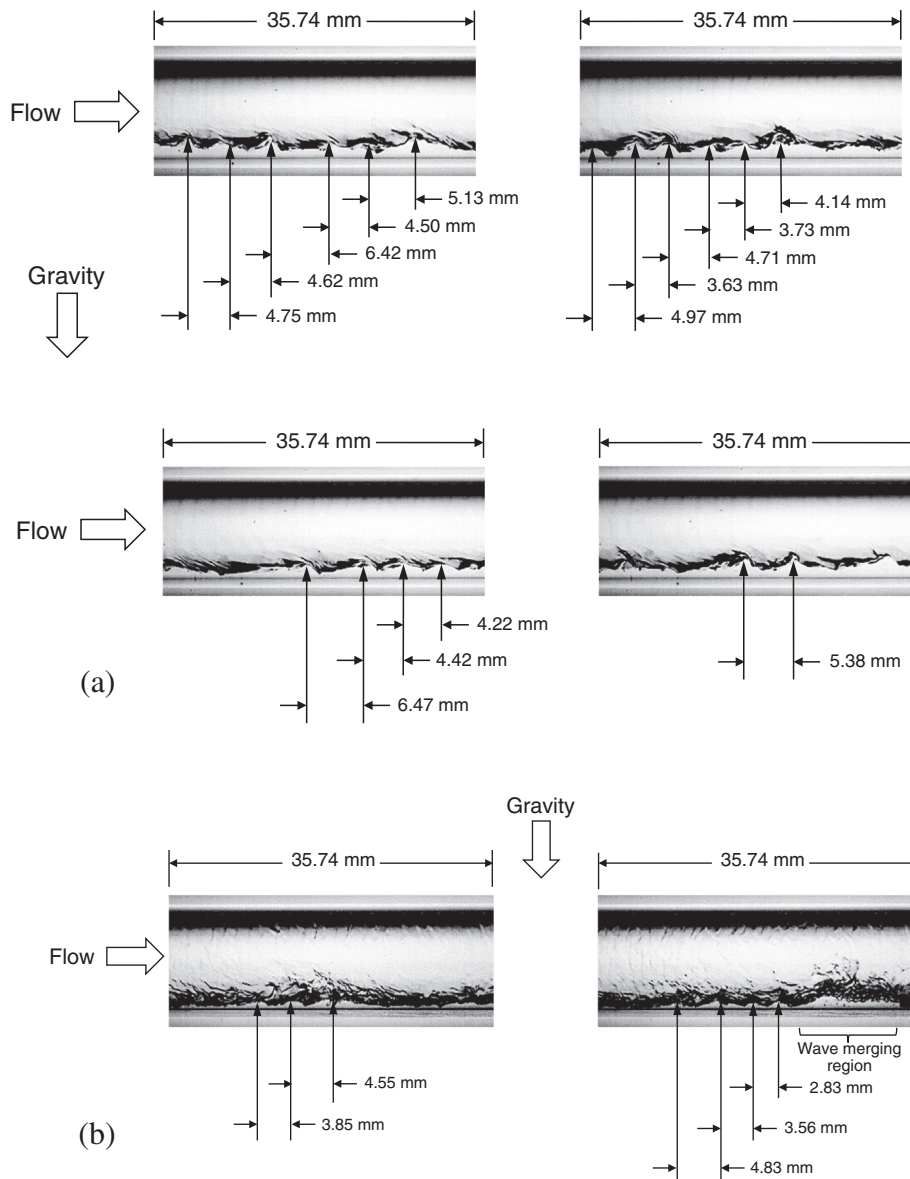
Fig. 6. Identification and measurement of interfacial wavelengths for horizontal flow condensation with (a) G_{FC} = 39.94 kg/m^2 s and (b) G_{FC} = 79.78 kg/m^2 s.

with gravity influence for $1.61 \leqslant j_g^* < 2.54$, and wavy-annular without gravity influence for $j_g^* \geqslant 2.54$.

For vertical downflow condensation, an outlet film Reynolds number of $Re_{f,out}$ = 770 is used as the transition value separating *laminar annular* and *turbulent annular* regimes as discussed in [28].

For vertical upflow condensation, flow regimes are determined using transition boundary relations based on dimensionless superficial velocities of vapor and liquid, j_g^* and j_f^*, respectively, where $j_f^* = (1 - x_e)G_{FC}/\sqrt{gD_i\rho_g(\rho_f - \rho_g)}$ [30]. The transition boundaries are identified according to the relation $\sqrt{j_g^*} + \sqrt{j_f^*} = C$, and the flow regimes can be summarized as: *climbing film* for $C > 1.21$, *flooding* for $1.0 < C < 1.21$, *oscillating film* for $0.85 < C < 1.0$, and *falling film* for $C < 0.85$.

Full details on why each of the above transition correlations was selected over others available in the literature can be found in [28–30]. In the next section, the above transition parameters and relations are used to segregate the data obtained from the condensation module intended for heat transfer measurements.

4.3. Circumferential variations of heat transfer parameters

Fig. 8(a) shows axial variations of wall temperatures along the condensation tube measured by thermocouples installed on the top and bottom of the outer wall of the inner tube, $T_{wall,o,top}$ and $T_{wall,o,bottom}$, respectively, and the measured cooling water temperature, T_w, for four different sets of operating conditions in horizontal flow. Fitted temperature profiles using third-order polynomials based on these temperature measurements as well as the average of top and bottom wall temperatures are also shown. It is clear from this figure that the differences between top and bottom outer wall temperatures are more significant in the *stratified-wavy* and *stratified* regimes. This is due to the accumulation of liquid and better cooling toward the bottom of the tube. The maximum temperature differences between top and bottom wall temperatures in the *stratified-wavy* and *stratified* regimes are 2.59 and 2.71 °C, respectively. The temperature differences are comparatively smaller in the *wavy-annular without gravity influence* and *wavy-annular with gravity influence* regimes as the liquid film is spread circumferentially around the inner perimeter due to the increasing vapor
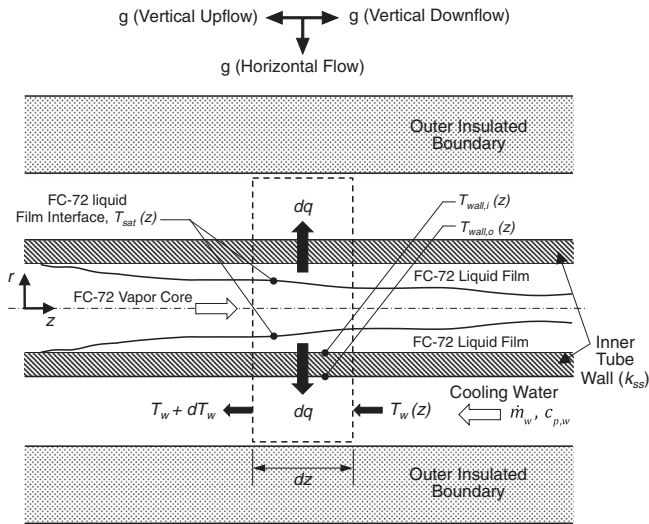
Fig. 7. Thermal model used to determine the local condensation heat transfer coefficient for FC-72.

shear. The maximum differences between top and bottom temperatures in the *wavy-annular without gravity influence* and *wavy-annular with gravity influence* regimes are 1.54 and 1.16 °C, respectively.

Unlike horizontal flow condensation, in which the direction of gravitational force is perpendicular to that of the flow, the differences between left and right wall temperatures for both vertical downflow and vertical upflow orientations are not significant as shown in Fig. 8(b) and (c). This is because the direction of gravitational force is parallel to the flow direction, which does not affect the circumferential symmetry of the liquid film. The maximum temperature differences between the left and right outer wall temperature measurements for vertical downflow and vertical upflow are 1.07 and 1.14 °C, respectively.

Axial variations of the condensation heat transfer coefficient for horizontal flow determined from top, bottom, and average wall temperatures are shown in Fig. 9(a) for the same operating conditions as those in Fig. 8(a). Similar to the temperature measurements for horizontal flow, more significant differences among the condensation heat transfer coefficients determined from the three wall temperatures are present in the *stratified-wavy* and *stratified* regimes. The maximum differences between condensation heat
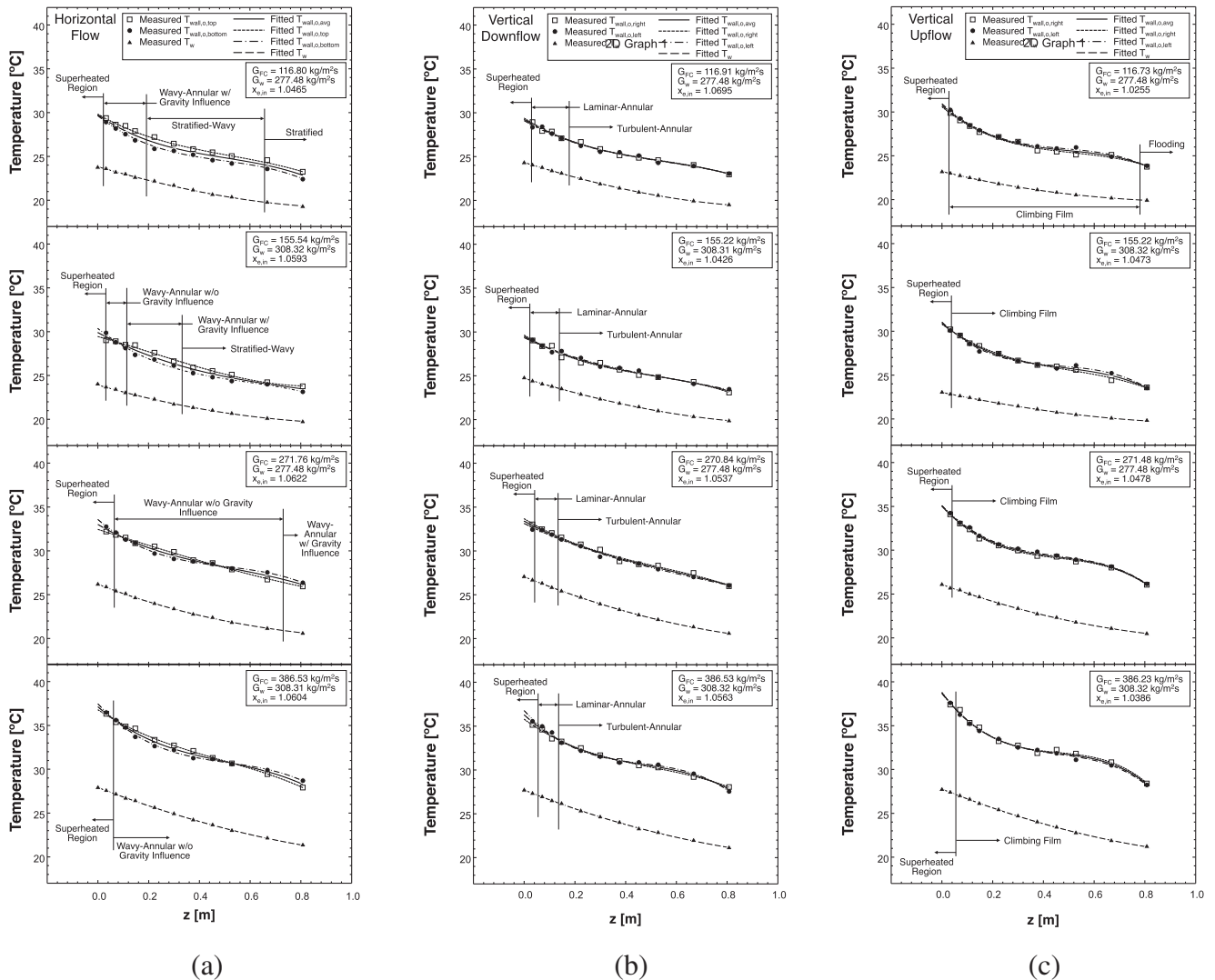

Fig. 8. Axial variations of inner tube wall temperatures and water temperature for different mass velocities for (a) horizontal flow, (b) vertical downflow, and (c) vertical upflow.
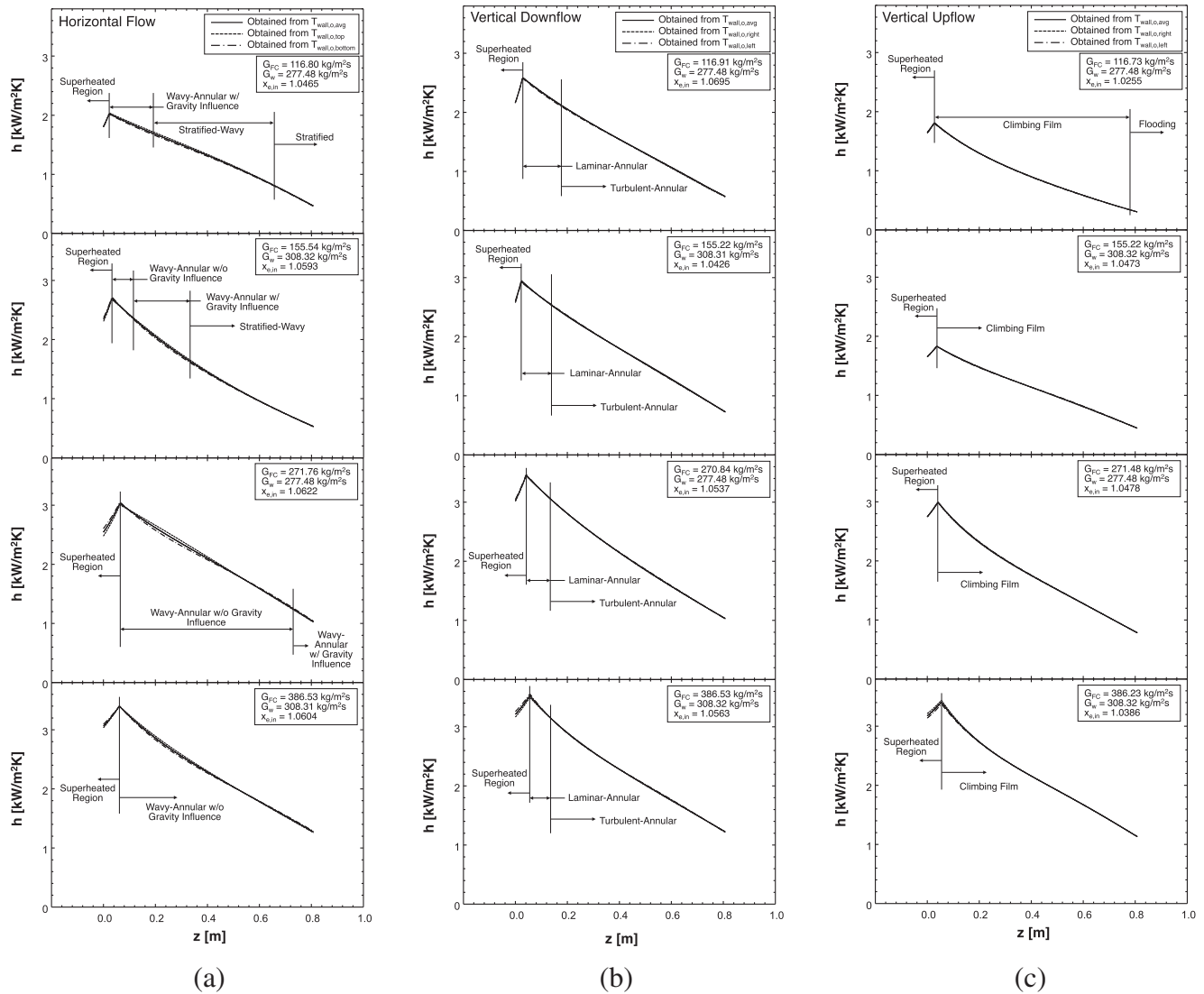
Fig. 9. Axial variations of condensation heat transfer coefficient for different mass velocities for (a) horizontal flow, (b) vertical downflow, and (c) vertical upflow.

transfer coefficients based on top versus bottom wall temperatures in the *stratified-wavy* and *stratified* regimes are 7.57% and 7.81%, respectively. The maximum differences between heat transfer coefficients in the *wavy-annular without gravity influence* and *wavy-annular with gravity influence* regimes are 4.60% and 3.22%, respectively.

Due to the small differences between left and right wall temperatures present in Fig. 8(b) and (c), differences between condensation heat transfer coefficients obtained using the left and right wall temperatures are relatively small for both vertical downflow and vertical upflow orientations as shown in Fig. 9(b) and (c), respectively. The maximum differences between heat transfer coefficients determined based on left and right wall temperatures for vertical downflow and vertical upflow are 3.08% and 3.19%, respectively.

It is important to note that all heat transfer results presented hereafter are based on the average of the two outer wall temperatures.

4.4. Heat transfer trends

Fig. 10(a) shows, for all three orientations, the amount of heat transferred from the FC-72 to the water per unit length, *dq/dz*, cal-

culated using average wall and water temperature curve fits and Eqs. (1) and (2). For all three orientations, *dq/dz* is highest in the upstream region where the condensate film is thinnest, and decreases gradually towards the downstream region with increased film thickens. Overall magnitudes of *dq/dz* increase with increasing FC-72 mass velocity due to the increased vapor shear providing higher film velocity.

Fig. 10(b) shows FC-72 mass quality, *x*, calculated using the previous information and $x = (\dot{m}_{FC} - \dot{m}_f)/\dot{m}_{FC}$ for all three flow orientations. As expected, these values are at their maximum in the superheated inlet region, and decrease towards the outlet. The rate of decrease is directly related to the amount of heat transferred per unit length shown in Fig. 10(a).

Fig. 10(c) shows axial variations of the experimentally determined local FC-72 heat transfer coefficient, *h*, in both the single-phase superheated vapor region and the two-phase condensation region for all three orientations, computed using average wall and water temperature curve fits. The heat transfer coefficients for all three flow orientations increase sharply in the superheated region near the inlet, and reach peak values where the liquid film is initiated. While a clearly defined single-phase vapor flow region before the peak point should yield a fairly constant *h* value, the trend of increasing *h* in the upstream region may be explained
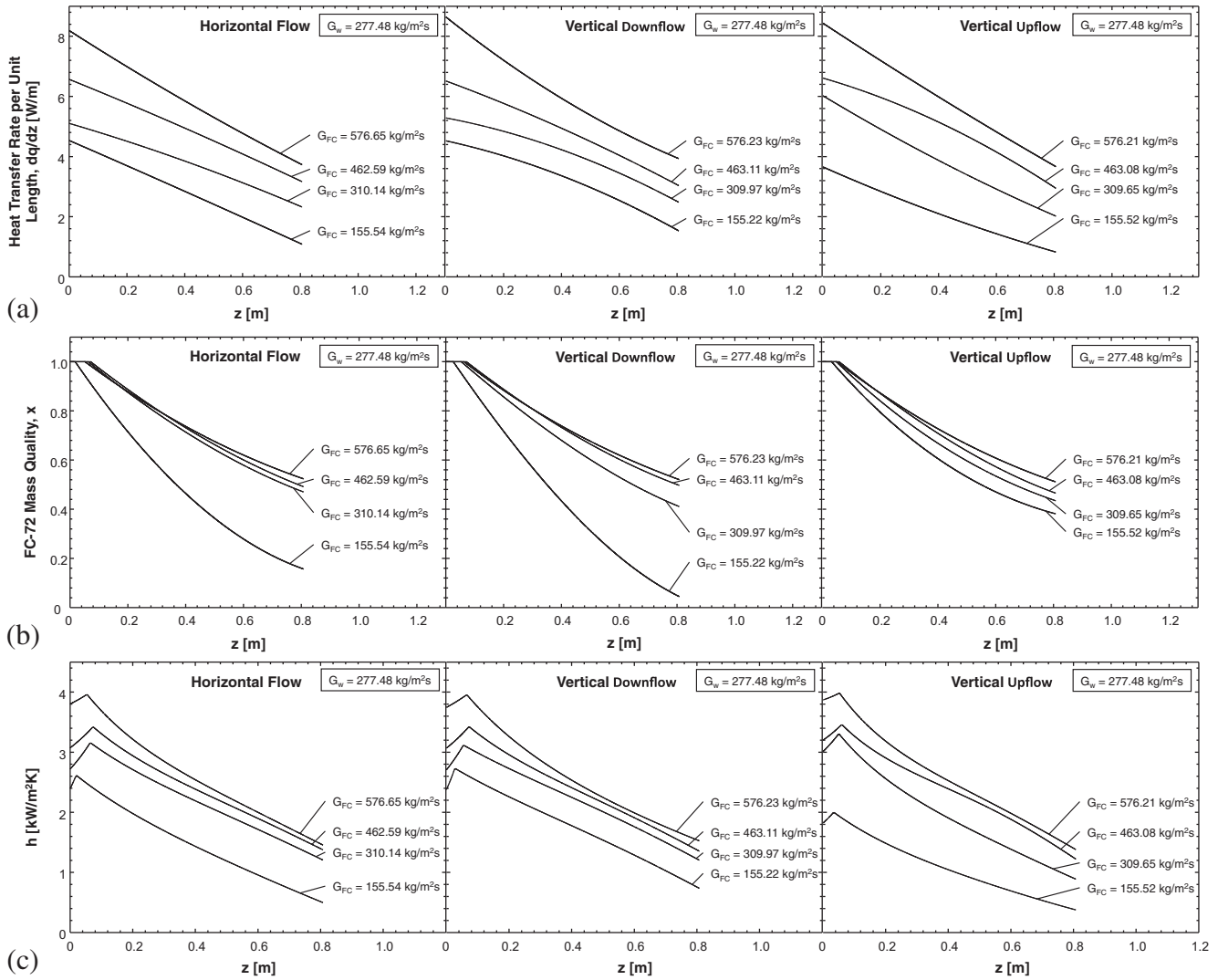
Fig. 10. Axial variations of (a) heat transfer rate per unit length, (b) FC-72 mass quality, and (c) heat transfer coefficient for all three orientations.

by film condensation commencing in a circumferentially nonuniform manner within the predominantly single-phase vapor region where $x_e > 1$. The peak value is believed to occur when the liquid film begins to fully cover the inner circumference. Fig. 10(c) also shows h decreases downstream of the peak value for all three flow orientations and all FC-72 mass velocities as the thickness of the liquid film gradually increases along the axial length. It also shows overall magnitude of h increases with increasing G_{FC} due to the thinning of the liquid film resulting from the increasing vapor shear.

4.5. Comparison of heat transfer coefficients for different flow orientations

Fig. 11 compares local condensation heat transfer coefficients for the three flow orientations and five sets of operating conditions. Fig. 11(a) and (b) are for relatively low FC-72 mass velocities of $G_{FC} = 116.80$ kg/m²s and $G_{FC} = 232.96$ kg/m²s, respectively. As shown in these figures, vertical downflow condensation achieves the highest h values, followed by horizontal flow and vertical upflow. Even though the flow images shown earlier in Fig. 5 with FC-72 mass velocities of $G_{FC} = 132.95$, 136.51, and 132.97 kg/m²s for horizontal flow, vertical downflow, and vertical upflow, respectively, show seemingly similar film behavior, the local condensa-

tion heat transfer coefficients shown in Fig. 11(b) for an even higher FC-72 mass velocity of $G_{FC} = 232.96$ kg/m²s exhibit measureable differences in h among the three flow orientations. It is believed that gravitation force at this FC-72 mass velocity has a measurable influence on liquid film velocity despite the film behavior appearing visually similar for all three flow orientations, thus affecting the magnitude of the heat transfer coefficient.

As the mass velocity of FC-72 is increased further to $G_{FC} = 386.53$ kg/m²s, Fig. 11(c), the axial variations and magnitudes of h are nearly identical for horizontal flow and vertical downflow, but the magnitude for vertical upflow is slightly lower. For the two highest FC-72 mass velocities of $G_{FC} = 424.59$ and 576.65 kg/m²s, Figs. 11(d) and 10(e), respectively, show gravitational force has virtually no influence on h, evidenced by all three flow orientations appearing to overlap with one another. This behavior may be explained by the high FC-72 mass velocities greatly increasing interfacial shear, and therefore dwarfing any gravitational effects.

Looking ahead, further understanding of annular film behavior may benefit from the use of new diagnostic tools. Previous studies at the Purdue University Boiling and Two-Phase Flow Laboratory (PU-BTPFL) have revealed the unique turbulence characteristics of liquid films, coupled with the complex interfacial waviness of films have profound effects on sensibly heated films [31], evaporating films [32], and condensing films [33]. Understanding these
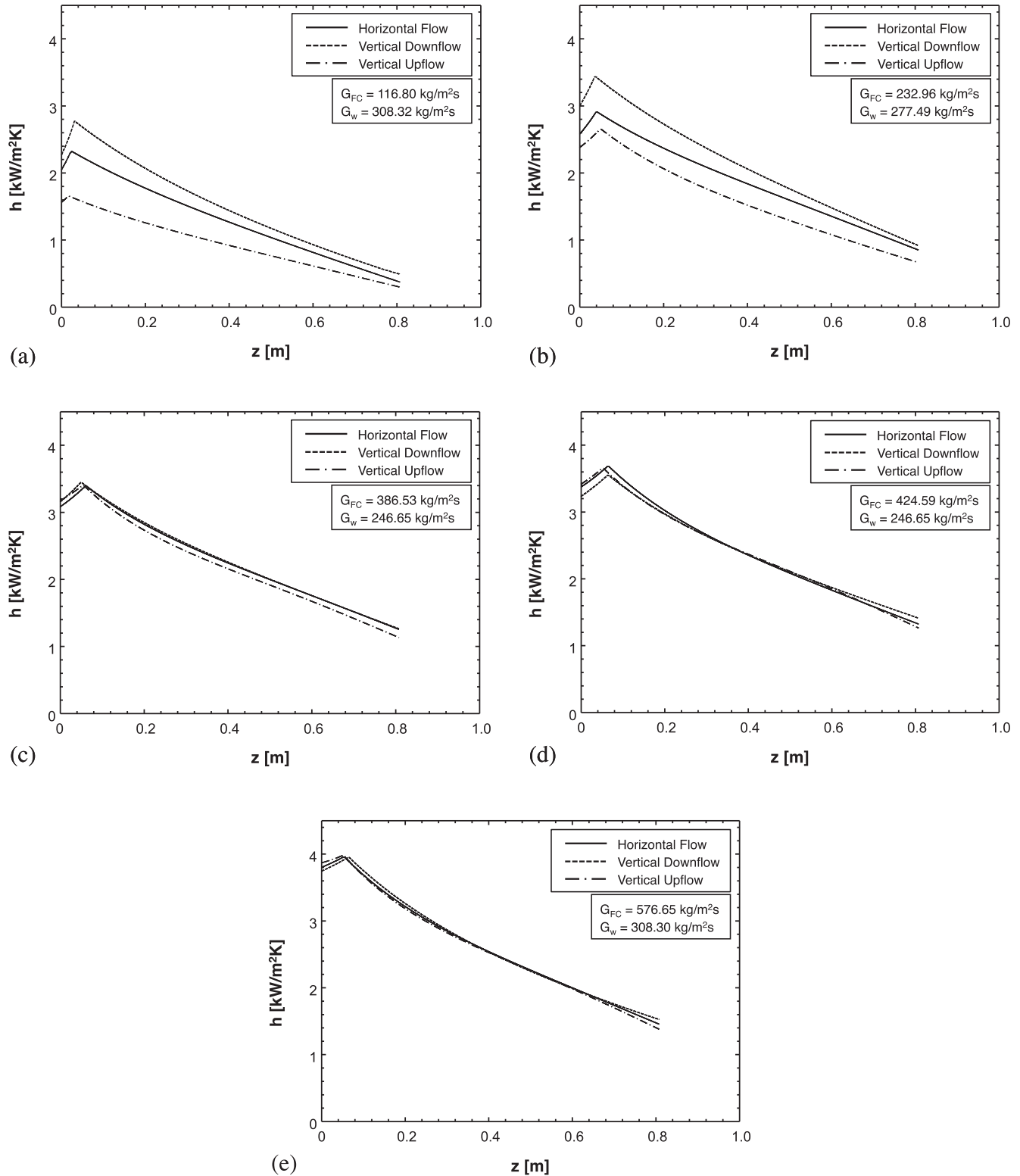
Fig. 11. Comparison of axial variations of experimentally determined condensation heat transfer coefficients for three flow orientations for (a) G_{FC} = 116.80 kg/m² s and G_w = 308.32 kg/m² s, (b) G_{FC} = 232.96 kg/m² s and G_w = 277.49 kg/m² s, (c) G_{FC} = 386.53 kg/m² s and G_w = 246.65 kg/m² s, (d) G_{FC} = 424.59 kg/m² s and G_w = 246.65 kg/m² s, and (e) G_{FC} = 576.65 kg/m² s and G_w = 308.30 kg/m² s.

complex phenomena will require accurate measurements of the film's velocity and temperature profiles, turbulence intensity across the film, and interfacial waviness. Such measurements are highly complicated by the small thickness of shear-driven annular condensing films, and are also sensitive to intrusive measurement

probes. Diagnostic techniques have also been developed to measure film thickness, temperature profile, and wave speed for heated free-falling films [34,35]. Methods to measure velocity profile and turbulence intensity have been employed, albeit for relatively thick adiabatic liquid films, using a combination of Laser Doppler

Velocimetry (LDV) and film thickness probes [36,37]. More accurate measurements of velocity profile and turbulence intensity across thin films are now possible with the aid of Micro-Particle Image Velocimetry (μ-PIV) techniques [38].

The findings from this study will be examined further in the second part of the study [23] in pursuit of mechanistic dimensionless criteria for negating the influence of gravity on flow condensation.

5. Conclusions

This study explored condensation of FC-72 in a circular tube for horizontal flow, vertical downflow, and vertical upflow. Two separate test modules were used, one for flow visualization purposes and the other for obtaining detailed heat transfer measurements. Using the flow visualization module and high-speed video motion analysis, the behavior of the condensate film and influence of gravity were investigated for different combinations of FC-72 and cooling water mass velocities at all three orientations. The condensation module for heat transfer measurements provided detailed axial and circumferential variations of the condensation heat transfer coefficient for the three flow orientations. Local and average condensation heat transfer coefficients for the three orientations were compared to assess the influence of body force on condensation heat transfer, and to determine the flow conditions that negate the influence of body force. Key findings from the study are as follows:

(1) Comparing flow images for different orientations shows very different liquid film behavior at relatively low and moderate FC-72 mass velocities, with horizontal flow yielding appreciable film stratification along the bottom of the tube, vertical downflow resulting in clearly separated annular flow, and vertical upflow exhibiting a combination of climbing annular film flow and flooding. On the other hand, flow behavior is virtually indistinguishable at high FC-72 mass velocities, with all three orientations yielding clearly separated annular flow.

(2) At low FC-72 mass velocities, the three orientations yield significant differences in heat transfer performance, with horizontal flow exhibiting sizable circumferential nonuniformities due to liquid stratification, and vertical downflow and vertical upflow yielding large differences in heat transfer coefficient because of body force alternatively aiding and hindering film motion, respectively. As FC-72 mass velocity is increased and interfacial shear begins to overcome body force, values of local heat transfer coefficients tend to converge for the three orientations, with mass velocities in the range of G_{FC} = 424.59–576.65 kg/m^{2}s exhibiting virtually no differences in heat transfer coefficient.

Acknowledgements

References

[1] J.M. Mandhane, G.A. Gregory, K. Aziz, A flow pattern map for gas–liquid flow in horizontal pipes, Int. J. Multiphase Flow 1 (1974) 537–553.

[2] G. Breber, J. Palen, J. Taborek, Prediction of horizontal tube-size condensation of pure components using flow regime criteria, in: J. Heat Transfer – Trans. ASME 102 (1980) 471–476.

[3] H.M. Soliman, On the annular-to-wavy flow pattern transition during condensation inside horizontal tubes, Can. J. Chem. Eng. 60 (1982) 475–481.

[4] H.M. Soliman, The mist-annular transition during condensation and its influence on the heat transfer mechanism, Int. J. Multiphase Flow 12 (1986) 277–288.

[5] A. Miyara, K. Nonaka, M. Taniguchi, Condensation heat transfer and flow pattern inside a herringbone-type micro-fin tube, Int. J. Refrig. 23 (2000) 141–152.

[6] Q. Chen, R.S. Amano, M. Xin, Experimental study of flow patterns and regimes of condensation in horizontal three-dimensional micro-fin tubes, Int. J. Heat Mass Transfer 43 (2006) 201–206.

[7] J.A. Olivier, L. Liebenberg, J.R. Thome, J.P. Meyer, Heat transfer, pressure drop, and flow pattern recognition during condensation inside smooth, helical micro-fin and herringbone tubes, Int. J. Refrig. 30 (2007) 609–623.

[8] S.M. Kim, I. Mudawar, Flow condensation in parallel micro-channels. Part 2: heat transfer results and correlation technique, Int. J. Heat Mass Transfer 55 (2012) 984–994.

[9] S. Lips, J.P. Meyer, Two-phase flow in inclined tubes with specific reference to condensation: a review, Int. J. Multiphase Flow 37 (2011) 845–859.

[10] H. Lee, I. Mudawar, M.M. Hasan, Experimental and theoretical investigation of annular flow condensation in microgravity, Int. J. Heat Mass Transfer 61 (2013) 293–309.

[11] D. Barnea, A unified model for predicting flow-pattern transitions for the whole range of pipe inclinations, Int. J. Multiphase Flow 13 (1987) 1–12.

[12] P.L. Spedding, J.J.J. Chen, V.T. Nguyen, Pressure drop in two phase gas-liquid flow in inclined pipes, Int. J. Multiphase Flow 8 (1982) 407–431.

[13] D.H. Beggs, J.P. Brill, A study of two-phase flow in inclined pipes, J. Pet. Technol. 25 (1973) 607–617.

[14] J.C. Chato, Laminar Condensation Inside Horizontal and Inclined Tubes (Doctoral dissertation), Massachusetts Institute of Technology, Cambridge, Massachusetts, 1960.

[15] B.X. Wang, X.Z. Du, Study on laminar film-wise condensation for vapor flow in an inclined small/mini-diameter tube, Int. J. Heat Mass Transfer 43 (2000) 1859–1868.

[16] M.A. Akhavan-Behabadi, R. Kumar, S.G. Mohseni, Condensation heat transfer of R-134a inside a microfin tube with different tube inclinations, Int. J. Heat Mass Transfer 50 (2007) 4864–4871.

[17] T. Nitheanandan, H.M. Soliman, Influence of tube inclination on the flow regime boundaries of condensing steam, Can. J. Chem. Eng. 71 (1993) 35–41.

[18] T. Nitheanandan, H.M. Soliman, Analysis of the stratified/nonstratified transitional boundary in horizontal and slightly inclined condensing flows, Can. J. Chem. Eng. 72 (1994) 26–34.

[19] S. Lips, J.P. Meyer, Experimental study of convective condensation in an inclined smooth tube. Part I: Inclination effect on flow pattern and heat transfer coefficient, Int. J. Heat Mass Transfer 55 (2012) 395–404.

[20] H.S. Wang, J.W. Rose, Film condensation in microchannels: effect of tube inclination, in: Proc. ASME 4th Int. Conf. on Nanochannels, Microchannels, and Minichannels, Limerick, Ireland, 2006, pp. 133–137.

[21] H. Saffari, V. Naziri, Theoretical modeling and numerical solution of stratified condensation in inclined tube, J. Mech. Sci. Technol. 24 (2010) 2587–2596.

[22] E. Da Riva, D. Del Col, Effect of gravity during condensation of R134a in a circular minichannel, Microgravity Sci. Technol. 23 (2011) 87–97.

[23] L.E. O'Neill, I. Park, C.R. Kharangate, V.S. Devahdhanush, V. Ganesan, I. Mudawar, Assessment of body force effects in flow condensation, Part II: Criteria for negating influence of gravity, Int. J. Heat Mass Transfer, in review.

[24] H. Zhang, I. Mudawar, M.M. Hasan, Experimental assessment of the effects of body force, surface tension force, and inertia on flow boiling CHF, Int. J. Heat Mass Transfer 45 (2002) 4079–4095.

[25] H. Zhang, I. Mudawar, M.M. Hasan, Experimental and theoretical study of orientation on flow boiling CHF, Int. J. Heat Mass Transfer 45 (2002) 4463–4477.

[26] H. Zhang, I. Mudawar, M.M. Hasan, A method for assessing the importance of body force on flow boiling CHF, J. Heat Transfer Trans. ASME 126 (2004) 161–168.

[27] H. Zhang, I. Mudawar, M.M. Hasan, Flow boiling CHF in microgravity, Int. J. Heat Mass Transfer 48 (2005) 3107–3188.

[28] I. Park, S.M. Kim, I. Mudawar, Experimental measurement and modeling of downflow condensation in a circular tube, Int. J. Heat Mass Transfer 57 (2013) 567–581.

[29] I. Park, H. Lee, I. Mudawar, Determination of flow regimes and heat transfer coefficient for condensation in horizontal tubes, Int. J. Heat Mass Transfer 80 (2015) 698–716.

[30] I. Park, I. Mudawar, Climbing film, flooding and falling film behavior in upflow condensation in tubes, Int. J. Heat Mass Transfer 65 (2013) 44–61.

[31] J.A. Shmerler, I. Mudawar, Local heat transfer coefficient in wavy free-falling turbulent liquid films undergoing uniform sensible heating, Int. J. Heat Mass Transfer 31 (1988) 67–77.

[32] J.A. Shmerler, I. Mudawar, Local evaporative heat transfer coefficient in turbulent free-falling liquid films, Int. J. Heat Mass Transfer 31 (1988) 731–742.

[33] S.M. Kim, I. Mudawar, Theoretical model for annular flow condensation in rectangular micro-channels, Int. J. Heat Mass Transfer 55 (2012) 958–970.

[34] T.H. Lyu, I. Mudawar, Statistical investigation of the relationship between interfacial waviness and sensible heat transfer to a falling liquid film, Int. J. Heat Mass Transfer 34 (1991) 1451–1464.

[35] T.H. Lyu, I. Mudawar, Determination of wave-induced fluctuations of wall temperature and convective heat transfer coefficient in the heating of a turbulent falling liquid film, Int. J. Heat Mass Transfer 34 (1991) 2521–2534.

[36] I. Mudawar, R.A. Houpt, Mass and momentum transport in smooth falling liquid films laminarized at relatively high Reynolds numbers, Int. J. Heat Mass Transfer 36 (1993) 3437–3448.

[37] I. Mudawar, R.A. Houpt, Measurement of mass and momentum transport in wavy-laminar falling liquid films, Int. J. Heat Mass Transfer 36 (1993) 4151–4162.

[38] W. Qu, I. Mudawar, S.-Y. Lee, S.T. Wereley, Experimental and computational investigation of flow development and pressure drop in a rectangular micro-channel, in: J. Electron. Packag. – Trans. ASME 128 (2006) 1–9.